Word Count: 9,432 words

Niobium speciation in minerals revealed by $L_{2,3}$-edges XANES spectroscopy (Revision 4)

Authors: Quentin Bollaert[1], Mathieu Chassé[1], Hebatalla Elnaggar[1,2], Amélie Juhin[1], Alexandra Courtin[3], Laurence Galoisy[1], Cécile Quantin[3], Marius Retegan[4], Delphine Vantelon[5], Georges Calas[1]

Affiliations:

[1]Sorbonne Université, Muséum National d'Histoire Naturelle, UMR CNRS 7590, IRD, Institut de Minéralogie, de Physique des Matériaux et de Cosmochimie, IMPMC, 75005 Paris, France.

[2]Debye Institute For Nanomaterials Science, Princetonplein 13584 CC Utrecht, The Netherlands.

[3]Université Paris Saclay, CNRS, UMR8148 GEOPS, 91405 Orsay Cedex.

[4]European Synchrotron Radiation Facility, 71, Avenue des Martyrs, 38000, Grenoble, France.

[5]Synchrotron SOLEIL, LUCIA beamline, L'Orme des Merisiers, Saint-Aubin BP48, 91192 Gif-sur-Yvette cedex, France.

ABSTRACT

The systematic mineralogy of niobium (Nb) is complex with more than one hundred species dominated by multicomponent oxides of similar chemistry. The determination of Nb speciation in solids (i.e. the distribution between the phases present and the crystal-chemical environment of Nb) is thus a challenge in geological contexts. Here, we present the first Nb $L_{2,3}$-edges X-ray absorption near-edge structure (XANES) measurements on a variety of Nb minerals and synthetic oxides with geological relevance. The interpretation of Nb $L_{2,3}$-edges XANES spectra in the light of crystal-field theory shows the sensitivity of spectra to local site symmetry and electronic environment around Nb atoms. Crystal-field multiplet simulations give estimates of the 10*Dq* crystal-field parameter values for Nb^{5+}, which range from 2.8 to 3.9 eV depending on Nb coordination and Nb–O distances. Rather than a 10*Dq* vs. R^{-5} relationship (where R represents the average Nb–O bond distance) expected in a point-charge model, we find a R^{-3} dependence with the crystal-field splitting for reference materials with octahedrally-coordinated Nb. Complementary ligand-field multiplet simulations provide evidence of charge transfer between Nb and O. The contribution of the ionic and covalent characters to the Nb–O bonds is equivalent, unlike more ionic 3*d* metal–O bonds. This systematic characterization of the $L_{2,3}$-edges XANES spectral properties of Nb provides information on the mechanisms by which Nb^{5+} substitutes for Fe^{3+}, Ti^{4+} or Ce^{4+} in oxides common in geological contexts. Whereas the substitution of Nb^{5+} for Ce^{4+} does not modify the local structure of the cation site in cerianite, the substitution of Nb^{5+} for Ti^{4+} in rutile and anatase results in an increase of the cation-ligand distance and a decrease in the symmetry of the cation site. Conversely, the substitution of Nb^{5+} for Fe^{3+} in hematite and goethite results in a smaller cation site distortion. Our study demonstrates the usefulness of $L_{2,3}$-edges XANES spectroscopy to determine Nb speciation in minerals in order to understand the processes of enrichment of this critical metal.

Keywords: Niobium, XANES, multiplet, 10*Dq*, local structure, speciation

INTRODUCTION

Niobium (Nb) is a quintessential critical element (European Commission 2020) used to manufacture superalloys, superconducting magnets and catalysts (Schulz et al. 2017). Niobium-based materials are also valued for the implementation of low-carbon technologies thanks to the unusual properties that arise from defects in their crystal structure (Ismael 2020, Ma et al. 2020). An increasing range of applications is expected to drive the future demand for Nb. This economic importance is exacerbated by the scarcity of Nb deposits. The incorporation of Nb into most common rock-forming minerals is limited by its low concentration on Earth (ca. 12 ppm in the upper continental crust; Rudnick and Gao 2003) and its geochemical properties. Only Nb^{5+} occurs under oxygen fugacities relevant to lithospheric and surficial environments (Cartier et al. 2015), with the electronic configuration [Kr] $4d^0$. This high valence and small ionic radius (0.64 Å in octahedral coordination; Shannon 1976) makes Nb a high-field-strength elements (HFSE) along with Zr, Sn, Hf, Ta, Pb, Th and U.

Niobium concentrates in silicic melts during partial melting and fractional crystallization until the precipitation of Nb minerals of the pyrochlore and columbite supergroups, which are among the last phases to form in most crystallization sequences (Linnen and Cuney 2005). When such rocks are exposed to weathering, the resistance of primary Nb minerals to alteration limits Nb leaching, making it one of the most immobile elements (Hill et al. 2000). Thus, it is used as a reference element for mass-balance calculations during weathering processes (Kurtz et al. 2000) or in environmental studies (Nabi et al. 2021). The formation of the largest Nb deposits is a consequence of this geochemical behavior, which leads to a significant residual enrichment during lateritic weathering of primary deposits, typically by an order of magnitude relative to the parent rock (Mitchell 2015).

Unambiguous identification of Nb minerals is needed to understand geological and geochemical processes concentrating Nb such as magmatic differentiation (Walter et al. 2018; Lee et al. 2006), metasomatic events (Wu et al. 2021) and supergene weathering (Lottermoser and

England 1988; Wall et al. 1996). However, the similar crystal chemistry and the frequent metamictization of Nb minerals make the analysis of Nb speciation using X-ray diffraction analyses challenging. The most abundant phases are multicomponent oxides with the general formulas AB_2O_6 (columbite-group minerals: e.g. columbite, euxenite, aeschynite) and $A_{2-x}B_2O_7$ (pyrochlore-group minerals: pyrochlore, betafite, samarskite). The eight-fold coordinated A-site, a square antiprism, can be occupied by rare-earth elements (REE), Ca, U, Th, Fe, while the octahedral B-site can be occupied by Ti, Nb, Ta and W and forms double chains in a zigzag pattern by sharing at least two edges with neighboring octahedra (Ewing 1975). Due to strong interionic repulsion, most NbO_6 octahedra are distorted (Kunz and Brown 1995). Metamictization is common due to the presence of radioactive elements (Zietlow et al. 2017). This process leads to the formation of local structures made of corner-sharing octahedra at the expense of the edge-sharing linkages observed in crystalline oxides (Ewing 1975).

Niobium is also found as a minor or trace element in oxide minerals. Hydrothermal events can produce amorphous Fe oxides containing low amounts of Nb (Wu et al. 2021). In metasomatized mantle peridotites, rutile may host more than 95 % of the Nb budget (Kalfoun et al. 2002). Niobium can also be enriched in Fe- and Ti oxides that occur as veinlets or weathering products in laterites (Lottermoser and England 1988; Giovannini et al. 2017). These oxides highlight the capacity of Nb^{5+} to substitute for cations such as Ti^{4+}, Sn^{4+}, W^{6+}, Ce^{4+} and Fe^{3+} in various minerals (Černý and Ercit 1989; Giovannini et al. 2017), which further complicates the determination of Nb speciation in such geological contexts.

Here, we report the first systematic analysis of Nb $L_{2,3}$-edges XANES spectra using a selected set of Nb minerals (fluorcalciopyrochlore, hydropyrochlore, niocalite, Nb perovskite, columbite) and synthetic oxides (Nb_2O_5, lueshite and Nb-substituted hematite, goethite, rutile, anatase and cerianite). So far, only a few $L_{2,3}$-edges XANES spectroscopic studies have been published on synthetic Nb oxides and fluorides (Sugiura et al. 1988; Kubouchi et al. 2012; Wang et al. 2018). The objectives of this work are thus twofold:

(1) To relate spectral properties to the local electronic structure of Nb in crystalline materials by means of crystal-field and ligand-field multiplet (CFM and LFM) calculations. Such an approach has proven to be useful to model the bioavailability and mobility of Fe in terrestrial and subsurface environments (Bhattacharyya et al. 2019) and V speciation in fresnoite (Höche et al. 2013).

(2) To investigate the processes by which Nb substitutes for Fe, Ti and Ce in oxides, which can serve as models for the major Nb-bearing oxides found in geological contexts and used in industry.

Overall, the present study on Nb speciation in geological contexts demonstrates how the sensitivity of Nb $L_{2,3}$-edges XANES spectroscopy can be used to better characterize and understand Nb mineralogy. In primary and lateritic deposits, deciphering Nb speciation will improve our understanding of Nb enrichment and may help to diversify the range of primary sources and to upgrade the efficiency of ore processing (Černý and Ercit 1989).

MATERIALS AND METHODS

Mineral synthesis procedures

Niobium-substituted Fe oxides (1 wt% Nb). The synthesis of Nb-bearing goethite (α-FeOOH) has been adapted from the hydrothermal synthesis of Sc-bearing Fe oxides at 70 °C (Chassé et al. 2017). Nb-bearing goethite was converted into Nb-bearing hematite (α-Fe_2O_3) by dehydroxylation at 300 °C for 2 h. The solid was washed using H_2SO_4 in order to remove potential adsorbed Nb species and poorly-crystallized material.

Niobium-substituted Ti oxides (5 wt% Nb). The synthesis of Nb-bearing anatase (TiO_2) has been carried out using a sol-gel method at moderate temperature (Dufour et al. 2012). Niobium-bearing rutile (5 wt%) was obtained by heating Nb-bearing anatase (5 wt%) at 700 °C for 3 hours. Niobium-bearing anatase samples with 1 and 10 wt% Nb were also synthesized following this procedure.

Niobium-substituted cerianite (1 wt% Nb). Niobium-bearing cerianite was synthesized using a high temperature solid-state reaction at 1,300 °C by homogenizing CeO_2, Nb_2O_5 and Nd_2O_3 powders (Olegário et al. 2013).

Lueshite. This reference material was obtained by following a hydrothermal synthesis procedure at 200 °C over 24 h based on the experimental procedure of Gouget et al. (2019).

Analytical methods

Powder X-ray diffraction (XRD) analyses. The successful completion of the syntheses was verified by X-ray diffraction analysis. X-ray diffraction was performed using a PANALYTICAL X'pert Pro MPD diffractometer. Measurements were carried out in Bragg-Brentano geometry using a Co Kα anode in order to minimize the X-ray absorption of Fe in hematite and goethite. Data were recorded with an X'Celerator detector between 3 °2θ and 90 °2θ with 0.017 ° steps. The incident beam mask was fixed at 20 mm and the Soller slits at 0.04 rad. Total counting time of measurement was 3 hours per sample. The crystal structure of synthetic compounds was checked using the International Centre for Diffraction Data (ICDD) references (PDF-2 database). No secondary niobian phase was detected on the XRD patterns of Nb-bearing Fe, Ti and Ce oxides confirming that the Nb ions were incorporated into the crystal lattice and substituted for Fe, Ce and Ti (Supplemental Figs. S1 and S2).

Single-crystal XRD. Single-crystal X-ray diffraction data were acquired on natural Nb reference materials using an Agilent Diffraction Xcalibur-S diffractometer equipped with a Sapphire CCD-detector with Mo *K*-α1 radiation (λ = 0.71073 Å, graphite monochromator) at 293 K. Data reduction, cell refinement and space group determination were performed using the CrysAlisPro software.

Electron microprobe (EMP) analyses. Electron microprobe (EMP) analyses were used to determine the crystal chemistry of the Nb reference materials sourced from mineralogical collections. Analyses were conducted on a CAMECA SX Five electron probe at the CAMPARIS facility (Sorbonne Université, Paris). After checking the homogeneity of the samples, two to seven

spots were probed on each sample at 15 kV and 40 nA for the major elements and at 15 kV and 299 nA for minor and trace elements. Wavelength-dispersive spectroscopy analyses were performed using the following standards: albite for Na, diopside for Mg, Si and Ca, orthoclase for Al and K, $MnTiO_3$ for Mn and Ti, hematite for Fe, $BaSO_4$ for Ba, topaz for F, $LiNbO_3$ for Nb, metallic Ta for Ta, SrSi for Sr, zircon for Zr, galena for Pb, monazite for Th, uraninite for U and allanite-(Y) for Y, La, Ce, Nd.

Acquisition of X-ray absorption spectra. Niobium L_3-edge (2360–2390 eV) and L_2-edge (2455–2485 eV) XANES spectra were recorded on LUCIA beamline at SOLEIL synchrotron radiation facility (Gif-sur-Yvette, France) operating with a storage ring current of 450 mA and energy of 2.75 GeV (Vantelon et al. 2016). A Si(111) double-crystal monochromator was used with an energy resolution of 0.25 eV at 2400 eV (Schaefers et al. 2007). The monochromator was calibrated at the energy of the Nb L_3-edge using Nb_2O_5. Due to the high Nb content of Nb minerals, spectra were recorded on cellulose-diluted pellets before being mounted on a holder. Pure pellets were used for synthetic Nb-substituted samples. Data were collected between 2300 and 2550 eV at room temperature, under vacuum, in fluorescence mode. Energy steps were (2, 0.2, 1, 0.2, 1) eV for energy ranges of (2300–2350), (2350–2400), (2400–2455), (2455–2490) and (2490–2550) eV, respectively, with a 1 s integration time. Two measurements per sample were sufficient to obtain a good signal-to-noise ratio and check the reproducibility of the edge features.

Data processing and simulations

Processing of X-ray absorption data. Data were processed using the Larch software (Newville 2013). The MBACK normalization algorithm was applied to prevent distortion in the XANES data and preserve the branching ratio (Weng et al. 2005). This method applies a single smooth background function over the entire $L_{2,3}$-edges data range rather than normalizing each edge independently. The normalization function is a first order Legendre polynomial (Supplemental Fig. S3) and the edge energy chosen as the input parameter of the MBACK function implemented in Larch is 2371 eV. The spectra of Nb-substituted hematite, Nb-substituted goethite, lueshite and

niocalite were trimmed beyond 2475 eV because the S *K*-edge hides the high-energy features of the Nb L_2-edge.

Niobium $L_{2,3}$-edges XANES features were fitted using three pseudo-Voigt functions in order to quantitatively compare and retrieve differences in the three features between the spectra. The continuum background was removed using an error function with fixed inflection points (2373.0 and 2467.0 eV) and large width (ca. 8 eV) to reproduce the slow onset of the electronic continuum (Brotton et al. 2007). No agreement or convention exists regarding the parameters of the background functions (Henderson et al. 2014) but similar procedures have been applied to Fe $L_{2,3}$-edges (Bourdelle et al. 2013) and Zr $L_{2,3}$-edges (Jollivet et al. 2013). An error function was preferred over the commonly-used arctangent because its width is related to the instrumental resolution rather than to the lifetime of the excited state, which is not known a priori. Because the best mathematical fits were obtained for a relative weight of Lorentzian to Gaussian components between 0.8 and 1.0 depending on the spectra, this parameter was fixed to 0.9 in all fits for comparative purposes.

Calculations of crystal-field and ligand-field multiplets. Simulations of the Nb $L_{2,3}$-edges spectra were performed using the Crispy software as implemented in the Quanty library (Haverkort 2016; Retegan 2019). Two approaches were tested to reproduce the spectral features. The first is a CFM calculation which takes into account the crystal-field effects acting on Nb. Ligand-field multiplet calculations offer a more comprehensive model by including ligand-to-metal charge transfer, i.e. by mixing in the ground state the $4d^0$, $4d^1\underline{L}^1$, $4d^2\underline{L}^2$, $4d^3\underline{L}^3$ configurations through a hybridization Hamiltonian (more details on this notation are provided in Supplemental Material).

Crystal- and ligand-field multiplet calculations both require specific input parameters. To account for the lifetime broadening, Lorentzian functions with a full width at half-maximum of 1.66 eV and 1.87 eV for the L_3 and L_2-edges were used to simulate the features (Krause and Oliver 1979). The experimental Gaussian broadening was set to ca. 1.5 eV to best reproduce the experimental spectra. The simulations of the experimental spectra were carried out by finding the

best scaling factors for the Slater-Condon integrals that best account for direct and exchange interactions between the 2*p*–4*d* orbitals (F^2_{pd} = 2.680 eV, G^1_{pd} = 1.627 eV and G^3_{pd}= 0.946 eV for the free ion). The reduction of these values modifies the relative intensity of the features. The values of the 4*d* and 2*p* spin-orbit coupling parameters were kept close to the atomic values of 0.124 eV and 63.97 eV. The crystal-field splitting parameter (10*Dq*) was chosen to best reproduce the energy difference between the two features, which corresponds to the splitting of the final state of the *d* orbitals. The extra parameters required for LFM calculations are the hybridization strength V_{mix} (V_{t2g}, V_{eg}), the configuration-averaged energies of the charge transfer configuration (E($4d^1\underline{L}^1$)–E($4d^0$)) Δ, the core-hole potential U_{dc} and the average Coulomb interaction energies of a corresponding electron pair U_{dd}. Detailed explanations of these parameters and their influence on the spectral shapes are given in Supplemental Material (Supplemental Fig. S7).

RESULTS

Characteristics of niobium $L_{2,3}$-edges XANES spectra

The Nb $L_{2,3}$-edges XANES spectra (Fig. 1) are characterized by a split edge feature with two peaks (A and B features) followed by a peak of lower intensity, ca. 10 eV after the edge (C feature), as reported for other Nb-bearing materials (Sugiura et al. 1988; Wang et al. 2018). The energy of the L_3-edge features (A_3, B_3, C_3) varies around ca. 2372, 2376 and 2387 eV, respectively (Fig. 1a). The energy of the L_2-edge features (A_2, B_2, C_2) varies around ca. 2466, 2470 and 2481 eV, respectively (Fig. 1b). At the L_3-edge, the energy position and width of the A_3 feature are stable. For the B_3 features, these characteristics are prone to variations depending on the reference materials. The spectra of niocalite, Nb-substituted hematite and Nb-substituted goethite show narrower B_3 features than the other reference materials. In contrast, the wide B_3 feature of Nb perovskite spectra shows a shoulder at high energy (B'_3 at 2379–2380 eV, Fig 2h). In all compounds, C_3 is of lower intensity than A_3 and B_3 with limited variation in position and width. Similar trends are observed at the L_2-edge.

Analysis of the niobium $L_{2,3}$-edges XANES spectra

Variation of the edge splitting. The ΔE parameter, corresponding to the energy splitting between the A and B features, ranges from ca. 2.6 to 4.0 eV at the L_3-edge and from ca. 2.3 to 4.0 eV at the L_2-edge (Table 2). Lueshite, Nb perovskite, fluorcalciopyrochlore and hydropyrochlore spectra have the largest ΔE values (ranging from ca. 3.6 to 4.0 eV). Most spectra have ΔE values between ca. 3.1 and 3.5 eV except for Nb-substituted cerianite spectra (ca. 2.6 and 2.3 eV at the L_3- and L_2-edges, respectively). Overall, the energy splitting at the L_3-edge follows the same trend ($R^2 = 0.94$) as the energy splitting at the L_2-edge (Supplemental Fig. S6a).

Variation of the intensity ratio. The intensity ratio between the A and B features (I_A/I_B) varies between ca. 0.8 and 2.1. It is higher at the L_2-edge (1.43) than at the L_3-edge (1.07). In most compounds, it ranges between ca. 1.0–1.2 and 1.4–1.6 at the L_3- and L_2-edges, respectively (Table 2). Intensity ratios of Nb-substituted cerianite and Nb_2O_5 spectra are below 1 at the L_3-edge (Fig. 2g). There is a strong positive correlation of this parameter between the two edges ($R^2 = 0.95$, Supplemental Fig. S6b).

Variation of the bandwidth. The ratio of the full width at half maximum of feature B with respect to feature A ($FWHM_{B/A}$), ranges between ca. 1.0 and 2.2 for both edges. The spectra of Nb-substituted goethite and hematite (Fig. 2c, 2d) have the lowest $FWHM_{B/A}$ values (ca. 1.1 and 1.4 at the L_3- and L_2-edges, respectively). Most spectra exhibit intermediate $FWHM_{B/A}$ values (ca. 1.4–1.7 and ca. 1.6–1.9 at the L_3- and L_2-edges, respectively). The spectra of Nb perovskite (Fig. 2h) stands out by its high $FWHM_{B/A}$ value (ca. 2.1 and 2.4 at the L_3-and L_2-edges, respectively). Niobium-substituted anatase spectra (Fig. 2f) are also characterized by high $FWHM_{B/A}$, especially at the L_2-edge (ca. 1.8–1.9 eV). On average, the width ratios at the L_3-edge (1.54) are smaller than those at the L_2-edge (1.73). The $FWHM_{B/A}$ parameter is correlated between the two edges ($R^2 = 0.93$ when the lueshite spectra are excluded as they deviate from the general trend, Supplemental Fig. S6c)

Multiplet calculations

Crystal-field multiplet calculations. The spectral features of Nb-substituted cerianite and

hematite are well reproduced by considering Nb in a regular polyhedron (O_h) (Figs. 3a and 3b) with crystal field values of 2.8 and 3.7 eV, respectively (Table 3). The spectra of hydropyrochlore and Nb perovskite are best modeled with a 10Dq value of 3.9 eV, which reproduces the splitting between the features (Figs. 3c and 3d). Nonetheless, the B' features of low intensity at 2379–2380 eV are absent. The good reproduction of the intensity ratios of the spectra for Nb-substituted cerianite, hematite and hydropyrochlore results from the reduction of the Slater-Condon integrals to 50 %, an indication that the contribution of the ionic and covalent characters to the Nb–O bonds is equivalent. The high intensity ratios of Nb perovskite spectra (Table 2) are reproduced with Slater-Condon integrals reduced to 35 %.

Ligand-field multiplet calculations. We calibrated our calculations using Nb-substituted hematite spectra, which exhibit the simplest spectral features. Charge-transfer parameters (U_{dc}, U_{dd}, Δ, V_{mix}, Table 4) were chosen according to calculations done on Ti^{4+} ($3d^0$)-compounds (Okada and Kotani 1993). The intensity of the features of Nb-substituted hematite spectra is improved and the C feature at ca. 2385 eV is reproduced when charge transfers are considered (Fig. 4). We also attempted to reproduce the B' features in the spectra of hydropyrochlore and Nb perovskite by investigating the influence of the hybridization strength (V_{mix}) on the spectral shapes. Using the same charge-transfer parameters, the LFM calculation fails to explain the coexistence of B' and C features visible on these spectra (Fig. 5).

DISCUSSION

$L_{2,3}$-edges XANES spectroscopy mirrors the electronic environment of niobium

Spectral energy splitting, interatomic distances and site symmetry. Niobium $L_{2,3}$-edges correspond to transitions to empty 4d states, making them sensitive to crystal-field effects. In the framework of crystal-field theory and given that O^{2-} is the ligand of Nb^{5+} in all of our reference materials, ΔE is correlated with the 10Dq crystal-field parameter, and therefore mirrors Nb^{5+} site geometry and ligand distances.

The ΔE values range between 3.3 and 4.0 eV for octahedrally-coordinated Nb^{5+}. The ΔE

variability among reference materials with Nb in octahedral environment is correlated with the average interatomic distances (R^2 = -0.80), as expected from the relationship between 10*Dq* and the inverse fifth power of the average interatomic distance (i.e. R^{-5}) (Fig. 6) in a point-charge model (Burns 1993). Nonetheless, the experimental data are best fitted with a function proportional to R^{-3} (χ^2 = 0.17), rather than a function proportional to R^{-5} (χ^2 = 0.26). Other studies indicate similar deviation from the expected theoretical R^{-5} dependence with crystal-field splitting ($R^{-8.3}$ in Lebernegg et al. 2008; R^{-2} in Wang et al. 2018). The energy splitting in the spectra of Nb-substituted Ti oxides deviates from both R^{-3} and R^{-5} models, reflecting the difference between probed Nb–O distances and theoretical Ti–O distances (Fig. 6).

Among reference materials with octahedral Nb, the spectra of Nb_2O_5 show the lowest ΔE values (3.06 and 3.28 eV at the L_2- and L_3-edges, respectively), slightly higher than previously reported (2.6 and 2.8 eV; Sugiura et al. 1988). Nb_2O_5 powders may differ from each other in the nature and proportion of the polymorphs they contain (Pilarek et al. 2017). Unfortunately, the material investigated by Sugiura et al. 1988 was not characterized by XRD. Our Nb_2O_5 reference consists of several polymorphs in equivalent proportions, with two monoclinic structures (ca. 90 % of NbO_6 octahedra and 10 % NbO_5 polyhedra: Andersson 1967) and an orthorhombic one (NbO_5 and NbO_7 polyhedra; Waring et al. 1973) (Supplemental Fig. S2c). The presence of these different structures leads to variations in the local environment of Nb which may explain a lower splitting as compared to the other octahedrally-coordinated Nb reference materials.

The ΔE value of cerianite spectra, in which Nb occupies a cubic site, is 6/9–7/9 times smaller than in reference materials containing octahedral Nb (Table 2). Indeed, crystal-field splitting values are lower than expected in cubic coordination ($10Dq_c$ is 8/9 of $10Dq_o$). Though not detected by XRD (Supplemental Fig. S2b), the synthesis of Nb-substituted cerianite can also result in the formation of trace amounts of tetrahedrally-coordinated fergusonite-(Ce) ([Ce, REE]NbO_4) due to the low solubility of Nb in cerianite (Kolodiazhnyi et al. 2016). The theoretical crystal-field splitting parameter of tetrahedral Nb^{5+} is even lower ($10Dq_t$ is 4/9 of $10Dq_o$) possibly explaining the

small ΔE value of spectra from cubic Nb-substituted cerianite.

The splitting of the main edge of $4d^0$ elements increases with increasing cation charge. For Zr^{4+}, Nb^{5+} and Mo^{6+} coordinated to oxygen ligands in weakly distorted octahedra, it is 3.2 eV (Galoisy et al. 1999), 3.5–3.9 eV (this study) and 4.5 eV (Bare et al. 1993), respectively. This trend highlights the decrease of the ionic radius with increasing cation charge ($^{[6]}Zr^{4+}$ = 0.72 Å, $^{[6]}Nb^{5+}$ = 0.64 Å, $^{[6]}Mo^{6+}$ = 0.59 Å; Shannon 1976) demonstrating the high sensitivity of $L_{2,3}$-edges XANES spectroscopy to the speciation of $4d^0$ elements.

Spectral broadening, charge transfer and site distortion. It is necessary to consider the C features in the fitting procedure in order to avoid an overestimation of the broadening of the B features. Unlike their assignment to $2p \rightarrow 5s$ transitions (Sugiura et al. 1988), our LFM calculations show that this feature results from hybridization between the 4*d* orbitals of Nb^{5+} and the 2*p* orbitals of O^{2-}, in agreement with the work of Okada and Kotani (1993) on Ti compounds.

The spectra of Nb minerals have a high-energy shoulder of varying intensity at 2378 eV. The high degree of distortion of NbO_6 octahedra in columbite and niocalite (Table 1) is not obvious from the fit of their XANES spectra. However, both compounds have a shoulder (labelled B') of limited intensity (Fig. 1). Furthermore, spectra of Nb perovskite and pyrochlore display the most intense B' shoulder yet these reference materials are composed of regular octahedra. The intensity of the shoulder is therefore not directly related to the distortion of the NbO_6 octahedra. Spectra of Nb perovskite exhibiting the most intense C feature are also those with the largest B' shoulder. We therefore ascribe the B' shoulder to orbital hybridization. The failure of ligand-field multiplet calculations to reproduce both B' and C features (Fig. 5) may be due to the differences between the Ti^{4+} charge-transfer parameters used here and those of Nb^{5+}, which are unknown (Okada and Kotani 1993).

The distortion of the cation site causes a broadening of the XANES features for Ti^{4+} and Zr^{4+} (De Groot et al. 1992; Ikeno et al. 2013; Jollivet et al. 2013). In contrast, the broadening of the Nb $L_{2,3}$-XANES features, probed by the $FWHM_{B/A}$ parameter, is determined by charge-transfer effects

and does not correlate with the degree of distortion of the NbO_6 octahedra. We conclude that the significant contribution of charge-transfer effects to Nb $L_{2,3}$-XANES spectra is related to the covalent character of the Nb–O bonds (Ikeno et al. 2011).

The spectra of Nb-substituted anatase and rutile display the poorest fit quality (χ^2 = 0.2–0.5) due to poor fitting of the wide B features characterized by slightly convex downward slopes. These compounds have a weak shoulder at 2378 eV, suggesting the limited effect of charge transfer on the spectra. In addition, another type of broadening is observed at the B feature (2376–2377 eV) which could reflect the distortion of the Nb sites (Fig. 2f). In contrast, only the spectra of Nb-substituted hematite and goethite exhibit A and B features of similar widths, suggesting a symmetrical Nb site rather than the low symmetry of Fe^{3+} expected in the highly distorted FeO_6 octahedra. This hypothesis is supported by the good reproduction of the spectra of Nb-substituted hematite in O_h symmetry using LFM calculations. Despite the different Fe environments and crystal structures of hematite and goethite, their spectral similarities indicate that the effect of distinct ligands (OH^- vs O^{2-}) or changes in the octahedra arrangements (face-, edge- or corner-sharing) are negligible compared to those of the site symmetry and average Nb–O distances.

Spectral intensity variations and bond covalence. The intensity ratios (I_A/I_B) exhibit low standard deviations in our dataset (σ = 0.13 and 0.20 at the L_3- and L_2-edges, respectively). The low intensity ratio of the L_3-edge spectrum of Nb-substituted cerianite (0.75) stands out from the other reference materials (1.10 on average for references with octahedrally-coordinated Nb). This can be explained by approximating the intensity ratio to the number of unoccupied states, i.e., 2/3 or 3/2 in regular cubic and octahedral coordination, respectively (Ogasawara et al. 2001). The intensity ratios retrieved from the fitting procedure are not equal to the statistical values because of ligand-field multiplet effects (Ogasawara et al. 2001). However, the intensity ratio at the L_2-edge of the reference materials with octahedrally-coordinated Nb is close to the statistical value of 3/2 (1.46 on average) because this edge is less affected by multiplet effects (De Groot, 1994).

The significance of multiplet effects can be estimated from our simulations through the

356 reduction factor of the Slater-Condon integrals. The range of values of the reduction factor (0.35–
357 0.54) indicates a major contribution from the covalent nature of the Nb–O bonds. These values are
358 remarkably low compared to those around 0.7–0.8 observed in most oxides of 3*d* elements (De
359 Groot 2005). The modeling of other Nb compounds, such as $CsNbF_6$, requires similar reduction of
360 these parameters down to 40 % (De Groot et al. 1994). Therefore, the reduction of the Slater-
361 Condon parameters mirrors the covalent nature of the bonds formed by 4*d* elements relative to 3*d*
362 elements (Singh et al. 2017).

363 **Why combine L_2- and L_3-edges XANES spectroscopy?** As the spectral features are
364 correlated between the L_2- and L_3-edges (Supplemental Fig. S5), the in-depth analysis of only one
365 edge is sufficient to determine the coordination number of Nb^{5+} and characterize the Nb local
366 environment. However, the simulation of XANES spectra using CFM and LFM calculations cannot
367 be carried out on a single edge. The lower sensitivity of the L_2-edge to atomic-multiplets effects
368 involves several pairs of solutions of the 10*Dq* value and the reduction of Slater integrals that
369 satisfactorily reproduce the L_2-edge spectra. Only the joint modeling of both edges constrains the
370 reduction of the Slater integrals, because of their higher sensitivity to atomic-multiplet effects (De
371 Groot et al. 1994). The choice for the acquisition and analysis of one or combined edges depends on
372 the precision of the crystallographic information one wants to extract from the spectra.

373 **Mechanisms of niobium substitution in oxides**

374 **Niobium-substituted Ti oxides.** The discrepancy between the average Ti–O distance in the
375 host structure and the observed Nb–O distances points out specific mechanisms of substitution in
376 Nb-substituted TiO_2 oxides (Fig. 6). Estimation of the Nb–O distances in Ti oxides by interpolation
377 of the correlation between ΔE and R^{-5} gives values of ca. 2.03 Å for Nb-substituted anatase and
378 ca. 2.01 Å for Nb-substituted rutile. Such an increase of the Nb–O distances is expected from the
379 larger ionic radius of Nb with respect to Ti ($^{[6]}Nb^{5+}$ = 0.64 Å and $^{[6]}Ti^{4+}$ = 0.605 Å; Shannon 1976).
380 Moreover, the symmetry of the Nb^{5+} site in TiO_2 is reduced as evidenced by the broadening of the
381 B_3 and B_2 features (Fig. 2f and Table 2). Increasing Nb substitution leads to lower ΔE and higher

382 $FWHM_{B/A}$ (Table 2), indicating an increased distortion of the Nb sites and increased Nb–O
383 distances. Such distortion of Nb sites and an increase in Nb–O distances with increasing amounts of
384 Nb were also evidenced using EXAFS (1.98 Å and 1.99 Å for $Ti_{0.97}Nb_{0.03}O_2$ and $Ti_{0.92}Nb_{0.08}O_2$,
385 respectively; Gardecka et al. 2015). The mechanism allowing the incorporation of Nb^{5+} in rutile and
386 anatase is the formation of one Ti^{4+} vacancy for every four Nb^{5+} (Sheppard et al. 2006) following
387 conditions of equilibrium and electroneutrality as illustrated by the Kröger-Vink notation:

388 $$5[Ti_{Ti}^{x}] + 2[Nb_2O_5] = 4[Nb_{Ti}^{\bullet}] + [V_{Ti}^{''''}] + 5[TiO_2] \quad (1)$$

389 In geological environments, the substitution of Nb^{5+} for Ti^{4+} in Ti oxides is also expected to be
390 accommodated by interstitial Fe^{3+} in oxidized environments following the substitution
391 $2Ti^{4+} = Fe^{3+} + 2Nb^{5+}$ (Ruck et al. 1986) and by Fe^{2+} in reducing environments, according to
392 $3Ti^{4+} = Fe^{2+} + 2Nb^{5+}$ (Giovannini et al. 2020).
393 Recent EXAFS analyses have highlighted the splitting of the first shell into two Nb-O
394 contributions at 1.88 and 2.01 Å in Nb-substituted anatase (Ribeiro et al. 2020). The increase of
395 Nb–O distances up to ca. 2.01 Å in the latter study and this work could reflect the presence of
396 Nb_2O_5 clusters in Nb-substituted anatase and rutile (Atanacio et al. 2014), as the values of Nb–O
397 distances in Nb_2O_5 are also 2.01 Å (Table 1). Even if the formation of Nb_2O_5 clusters cannot be
398 excluded, the differences between the spectra of Nb_2O_5 and Nb-substituted TiO_2 (Table 2) indicate
399 that Nb clustering is not an important process.
400 **Niobium-substituted Fe oxides.** Octahedral Fe^{3+} and Nb^{5+} have similar ionic radii, 0.645 Å
401 and 0.64 Å, respectively. The substitution of Nb^{5+} for Fe^{3+} in goethite is isormorphous (Oliveira et
402 al. 2008). Charge balance may be maintained by substituting $5Fe^{3+}$ for $3Nb^{5+}$, which induces cation
403 vacancies. Our study shows that Nb-substituted Fe oxides can be reproduced by CFM and LFM
404 calculations in regular O_h site symmetry even though the initial Fe site has a C_3 symmetry (Figs. 3b
405 and 4b). The regularity of the NbO_6 octahedra is also supported by the absence of broadening of
406 features B_3 and B_2 (Fig. 2c). The alignment of their experimental ΔE values on the trend with
407 respect to theoretical Fe–O distances (Fig. 6) indicates that the average Nb–O distances are not

408 significantly modified with respect to the average Fe–O distances.

409 However, EXAFS data on Nb-substituted hematite indicate shorter Nb–O distances (1.87 and
410 2.05 Å) than the Fe–O distances in hematite (1.92 and 2.11 Å; Silva et al. 2009). The differences
411 between our results and those of Silva et al. (2009) could reflect the high amounts of Nb
412 incorporated in the Fe oxides they synthesized (5 and 10 wt% Nb) or the synthesis protocol. The
413 incorporation of Nb in Fe oxides may result in a symmetrization of the Nb site due to the relaxation
414 of the crystal structure around Nb arising from the induced cation vacancies.

415 **Niobium-substituted cerianite.** Charge and size differences (0.97 and 0.64 Å, for Ce^{4+} and
416 Nb^{5+} respectively; Shannon 1976) limit the substitution of Nb in cerianite. The substitution of Nb^{5+}
417 for Ce^{4+} was explained by the displacement of Nb^{5+} cations from ideal cubic symmetry, leading to
418 oxygen vacancies (Hiley et al. 2018). It has also been suggested that half of the Ce ions become
419 trivalent to account for charge balance (Kolodiazhnyi et al. 2016). The other half of the charge
420 compensation would be accommodated by interstitial oxygens (Kolodiazhnyi et al. 2016, Schaube
421 et al. 2019) according to:

422 $$[Nb_2O_5] + 2[Ce_{Ce}^{x}] = 2[Nb_{Ce}^{\bullet}] + [O_i''] + 2[CeO_2] \quad (2)$$

423 Our simulation of Nb-substituted spectra in O_h point symmetry (Fig. 3a) indicates that a Nb^{5+}–
424 Nd^{3+} co-doping eases the charge balance equilibrium ($2[Ce^{4+}] = [Nb^{5+}] + [Nd^{3+}]$) and prevents
425 significant distortion of the Nb site by limiting the formation of interstitial oxygen and vacancies.

426 ## IMPLICATIONS

427 ### Deciphering the origin of the properties of technological Nb-substituted materials

428 Some of the synthetic Nb-bearing oxides investigated in this study are meeting technological
429 challenges associated with climate change mitigation or environmental decontamination (e.g.,
430 Ismael 2020; Ma et al. 2020). Among other applications, they are used for dye-sensitized solar cells
431 (Lü et al. 2010), Na-ion battery anodes (Usui et al. 2015), direct solar-to-fuel conversion (Fu et al.
432 2016), and catalysts for the removal of exhaust-gas nitrogen oxide (Lian et al. 2015). These

433 enhanced physico-chemical properties result from the presence of substituted Nb^{5+} leading to oxide
434 mobility and transport properties due to charge unbalancing, interstitial oxygen or vacancies. The
435 properties of these Nb materials may be rationalized by knowledge of the mechanisms of Nb
436 insertion, which can be unveiled by Nb $L_{2,3}$-edges XANES spectroscopy.

437 **Upgrading ore processing through quantitative Nb XANES spectroscopy**

438 The choice of Nb ore-processing strategies depends on the nature of the Nb minerals, their
439 degree of alteration and their crystal-chemical variability. It is essential to correctly characterize the
440 Nb ores to optimize ore processing (Černý and Ercit 1989). Niobium recovery from pyrochlore ores
441 using amine collectors is used in three processing plants worldwide (Guimarães and Weiss 2001).
442 Nevertheless, this process induces a significant loss of columbite and Nb-rutile between feed and
443 concentrate (Gibson et al. 2015). Moreover, a high concentration of Fe in pyrochlore, which is a
444 typical feature of hydropyrochlore, reduces its floatability and causes Nb loss during ore processing
445 (Chehreh Chelgani et al. 2012). Niobian rutile has also been identified in the world-class Nb deposit
446 of Araxá, but its significance in the overall Nb budget remains elusive (Neumann and Medeiros
447 2015). Therefore, Nb XANES spectroscopy may be a valuable tool for identifying Nb speciation in
448 ore minerals and optimizing ore-processing strategies.

449 **Unravelling Nb geochemical behavior in natural systems**

450 Recent findings in hydrothermal contexts (Andersson et al. 2018; Dietzel et al. 2019) and
451 near-surface conditions (Wall et al. 1996; Chakrabarty et al. 2013; Giovannini et al. 2017)
452 demonstrate the alteration of Nb minerals and question the presumed immobility of Nb (MacLean
453 and Barrett 1993). The sensitivity of Nb $L_{2,3}$-edges XANES spectroscopy opens the possibility to
454 track Nb mineral speciation in weathered Nb-enriched samples. It could also be used to determine
455 the mechanisms of alteration of primary Nb minerals and reveal the mechanisms of Nb
456 incorporation in newly-formed phases. A combination of bulk and micro-XANES analyses could
457 thus be used to enlighten the molecular-scale and geochemical factors that induce contrasted Nb

dynamics in supergene environments as has been done for rare-earth elements (Janots et al. 2015; Chassé et al. 2019; Borst et al. 2020).

ACKNOWLEDGEMENTS

We are grateful to Jean-Claude Boulliard and Éloïse Gaillou for the supply of rare mineral species from the Sorbonne Université and École Nationale Supérieure des Mines de Paris mineralogy (MINES ParisTech) collections. We thank Alain Demourgues and Guillaume Gouget for providing the niobate samples and commenting the manuscript, Sophie Cassaignon and Tsou Hsi Camille Chan Chang for the synthesis of Nb-substituted anatase, and Benoît Baptiste, Ludovic Delbes, Michel Fialin, and Nicolas Rividi for experimental support during XRD and EPMA analyses. We acknowledge SOLEIL for provision of synchrotron radiation facilities and thank the staff of the LUCIA beamline for their help in the measurement of Nb $L_{2,3}$-edges (Proposal No. 20191239).

REFERENCES

Andersson, S. (1967) The crystal structure of N-Nb_2O_5, prepared in the presence of small amounts of LiF. Zeitschrift für anorganische und allgemeine Chemie, 351, 106–112.

Andersson, S.S., Wagner, T., Jonsson, E., and Michallik, R.M. (2018) Mineralogy, paragenesis, and mineral chemistry of REEs in the Olserum-Djupedal REE-phosphate mineralization, SE Sweden. American Mineralogist, 103, 125–142.

Atanacio, A.J., Bak, T., and Nowotny, J. (2014) Niobium segregation in niobium-doped titanium dioxide (rutile). The Journal of Physical Chemistry C, 118, 11174–11185.

Bare, S.R., Mitchell, J.G.E., Maj, J.J., and Glands, J.L. (1993) Local site symmetry of dispersed molybdenum oxide catalysts: XANES at the Mo $L_{2,3}$-edges. The Journal of Physical Chemistry, 97, 6048–6053.

Bhattacharyya, A., Schmidt, M.P., Stavitski, E., Azimzadeh, B., and Martínez, C.E. (2019) Ligands representing important functional groups of natural organic matter facilitate Fe redox transformations and resulting binding environments. Geochimica et Cosmochimica Acta, 251, 157–175.

Borst, A.M., Smith, M.P., Finch, A.A., Estrade, G., Villanova-de-Benavent, C., Nason, P., Marquis, E., Horsburgh, N.J., Goodenough, K.M., Xu, C., and others (2020) Adsorption of rare earth elements in regolith-hosted clay deposits. Nature Communications, 11, 4386.

Bourdelle, F., Benzerara, K., Beyssac, O., Cosmidis, J., Neuville, D.R., Brown, G.E., and Paineau, E. (2013) Quantification of the ferric/ferrous iron ratio in silicates by scanning transmission X-ray microscopy at the Fe $L_{2,3}$ edges. Contributions to Mineralogy and Petrology, 166, 423–434.

Brotton, S.J., Shapiro, R., van der Laan, G., Guo, J., Glans, P.-A., and Ajello, J.M. (2007) Valence state fossils in Proterozoic stromatolites by L-edge X-ray absorption spectroscopy. Journal of Geophysical Research: Biogeosciences, 112(G3).

Burns, R.G. (1993) Mineralogical applications of crystal field theory, 2nd Ed., 551 p. Cambridge University Press, Cambridge, UK.

Cartier, C., Hammouda, T., Boyet, M., Mathon, O., Testemale, D., and Moine, B.N. (2015) Evidence for Nb^{2+} and Ta^{3+} in silicate melts under highly reducing conditions: A XANES study. American Mineralogist, 100, 2152–2158.

Černý, P., and Ercit, T.S. (1989) Mineralogy of niobium and tantalum: Crystal chemical relationships, paragenetic aspects and their economic implications. In P. Möller, P. Černý and F. Saupé, Eds., Lanthanides, tantalum and niobium, p. 27–79. Springer-Verlag, Berlin.

Chakrabarty, A., Mitchell, R.H., Ren, M., Sen, A.K., and Pruseth, K.L. (2013) Rinkite, cerianite-(Ce), and hingganite-(Ce) in syenite gneisses from the Sushina Hill Complex, India: Occurrence, compositional data and petrogenetic significance. Mineralogical Magazine, 77, 3137–3153.

Chassé, M., Griffin, W.L., O'Reilly, S.Y., and Calas, G. (2017) Scandium speciation in a world-class lateritic deposit. Geochemical Perspectives Letters, 3, 105–114.

Chassé, M., Griffin, W.L., O'Reilly, S.Y., and Calas, G. (2019) Australian laterites reveal mechanisms governing scandium dynamics in the critical zone. Geochimica et Cosmochimica Acta, 260, 292–310.

Chehreh Chelgani, S., Hart, B., Marois, J., and Ourriban, M. (2012) Study of pyrochlore matrix composition effects on froth flotation by SEM–EDX. Minerals Engineering, 30, 62–66.

De Groot, F.M.F (2005) Multiplet effects in X-ray spectroscopy. Coordination Chemistry Reviews, 249, 31–63.

De Groot, F.M.F, Figueiredo, M.O., Basto, M.J., Abbate, M., Petersen, H. and Fuggle, J.C. (1992) 2*p* X-ray absorption of titanium in minerals. Physics and Chemistry of Minerals, 19, 140–147.

De Groot, F.M.F., Hu, Z.W., Lopez, M.F., Kaindl, G., Guillot, F., and Tronc, M. (1994) Differences between L_3 and L_2 X-ray absorption spectra of transition metal compounds. The Journal of Chemical Physics, 101, 6570–6576.

Dietzel, C.A.F., Kristandt, T., Dahlgren, S., Giebel, R.J., Marks, M.A.W., Wenzel, T., and Markl, G. (2019) Hydrothermal processes in the Fen alkaline-carbonatite complex, southern Norway. Ore Geology Reviews, 111, 102969.

Dufour, F., Cassaignon, S., Durupthy, O., Colbeau-Justin, C., and Chanéac, C. (2012) Do TiO_2 nanoparticles really taste better when cooked in a microwave oven? European Journal of Inorganic Chemistry, 2012, 2707–2715.

European Commission (2020) Study on the EU's list of critical raw materials, Factsheets on critical raw materials; European Commission: Brussels, Belgium.

Ewing, R.C. (1975) The crystal chemistry of complex niobium and tantalum oxides: IV. The metamict state. Discussion. American Mineralogist, 60, 728–733.

Friis, H., and Casey, W.H. (2018) Niobium is highly mobile as a polyoxometalate ion during natural weathering. The Canadian Mineralogist, 56, 905–912.

Fu, Y., Dong, C.-L., Lee, W.-Y., Chen, J., Guo, P., Zhao, L., and Shen, S. (2016) Nb-doped hematite nanorods for efficient solar water splitting: Electronic structure evolution versus morphology alteration. ChemNanoMat, 2, 704–711.

Galoisy, L., Pélegrin, E., Arrio, M.-A., Ildefonse, P., Calas, G., Ghaleb, D., Fillet, C., and Pacaud, F. (1999) Evidence for 6-coordinated zirconium in inactive nuclear waste glasses. Journal of the American Ceramic Society, 82, 2219–2224.

Gardecka, A.J., Goh, G.K.L., Sankar, G., and Parkin, I.P. (2015) On the nature of niobium substitution in niobium doped titania thin films by AACVD and its impact on electrical and optical properties. Journal of Materials Chemistry A, 3, 17755–17762.

Gibson, C., Aghamirian, M., and Kelebek, S. (2015) Challenges in Niobium Flotation. In P. Blatter and J. Zinck, Eds., Proceedings of the 47th Annual Canadian Mineral Processors Operators Conference, p. 244-254. Canadian Institute of Mining, Metallurgy and Petroleum, Ottawa, Ontario, Canada.

Giovannini, A.L., Bastos Neto, A.C., Porto, C.G., Pereira, V.P., Takehara, L., Barbanson, L., and Bastos, P.H.S. (2017) Mineralogy and geochemistry of laterites from the Morro dos Seis Lagos Nb (Ti, REE) deposit (Amazonas, Brazil). Ore Geology Reviews, 88, 461–480.

Giovannini, A.L., Mitchell, R.H., Bastos Neto, A.C., Moura, C.A.V., Pereira, V.P., and Porto, C.G. (2020) Mineralogy and geochemistry of the Morro dos Seis Lagos siderite carbonatite, Amazonas, Brazil. Lithos, 360–361, 105433.

Gouget, G., Duttine, M., Chung, U.-C., Fourcade, S., Mauvy, F., Braida, M.-D., Le Mercier, T., and Demourgues, A. (2019) High ionic conductivity in oxygen-deficient Ti-substituted sodium niobates and the key role of structural features. Chemistry of Materials, 31, 2828–2841.

Guimarães, H.N., and Weiss, R.A. (2001) The complexity of the niobium deposits in the alkaline-ultramafic intrusions Catalao I and II - Brazil. Proceedings of international symposium on niobium, p. 37-51. Sao Paulo, Brazil.

Haverkort, M.W. (2016) *Quanty* for core level spectroscopy - excitons, resonances and band excitations in time and frequency domain. Journal of Physics: Conference Series, 712, 012001.

Haverkort, M.W., Zwierzycki, M., and Andersen, O.K. (2012) Multiplet ligand-field theory using Wannier orbitals. Physical Review B, 85, 165113.

Henderson, G.S., de Groot, F.M.F., and Moulton, B.J.A. (2014) X-ray absorption near-edge structure (XANES) spectroscopy. Reviews in Mineralogy and Geochemistry, 78, 75–138.

Hiley, C.I., Playford, H.Y., Fisher, J.M., Felix, N.C., Thompsett, D., Kashtiban, R.J., and Walton, R.I. (2018) Pair distribution function analysis of structural disorder by Nb^{5+} inclusion in ceria: Evidence for enhanced oxygen storage capacity from under-coordinated oxide. Journal of the American Chemical Society, 140, 1588–1591.

Hill, I.G., Worden, R.H., and Meighan, I.G. (2000) Geochemical evolution of a palaeolaterite: the Interbasaltic Formation, Northern Ireland. Chemical Geology, 166, 65–84.

Höche, T., Ikeno, H., Mader, M., Henderson, G.S., Blyth, R.I.R., Sales, B.C., and Tanaka, I. (2013) Vanadium $L_{2,3}$ XANES experiments and first-principles multielectron calculations: Impact of second-nearest neighboring cations on vanadium-bearing fresnoites. American Mineralogist, 98, 665–670.

Ikeno, H., Mizoguchi, T. and Tanaka, I. (2011) *Ab initio* charge transfer multiplet calculations on the $L_{2,3}$ XANES and ELNES of *3d* transition metal oxides. Physical Review B, 83, 155107.

Ikeno, H., Krause, M., Höche, T., Patzig, C., Hu, Y., Gawronski, A., Tanaka, I. and Rüssel, C. (2013) Variation of Zr-$L_{2,3}$ XANES in tetravalent zirconium oxides. Journal of Physics: Condensed Matter, 25, 165505.

Ismael, M. (2020) A review and recent advances in solar-to-hydrogen energy conversion based on photocatalytic water splitting over doped-TiO_2 nanoparticles. Solar Energy, 211, 522–546.

Janots, E., Bernier, F., Brunet, F., Muñoz, M., Trcera, N., Berger, A., and Lanson, M. (2015) Ce(III) and Ce(IV) (re)distribution and fractionation in a laterite profile from Madagascar: Insights from in situ XANES spectroscopy at the Ce L_{III}-edge. Geochimica et Cosmochimica Acta, 153, 134–148.

Jollivet, P., Calas, G., Galoisy, L., Angeli, F., Bergeron, B., Gin, S., Ruffoni, M.P., and Trcera, N. (2013) An enhanced resolution of the structural environment of zirconium in borosilicate glasses. Journal of Non-Crystalline Solids, 381, 40–47.

Kalfoun, F., Ionov, D., and Merlet, C. (2002) HFSE residence and Nb/Ta ratios in metasomatised, rutile-bearing mantle peridotites. Earth and Planetary Science Letters, 199, 49–65.

Kolodiazhnyi, T., Sakurai, H., Belik, A.A., and Gornostaeva, O.V. (2016) Unusual lattice evolution and magnetochemistry of Nb doped CeO_2. Acta Materialia, 113, 116–123.

Krause, M.O., and Oliver, J.H. (1979) Natural widths of atomic *K* and *L* levels, *K*α X-ray lines and several *KLL* Auger lines. Journal of Physical and Chemical Reference Data, 8, 329–338.

Kubouchi, Y., Hayakawa, S., Namatame, H., and Hirokawa, T. (2012) Direct observation of fractional change of niobium ionic species in a solution by means of X-ray absorption fine structure spectroscopy: XAFS spectroscopy of solutions. X-Ray Spectrometry, 41, 259–263.

Kunz, M., and Brown, I.D. (1995) Out-of-center distortions around octahedrally coordinated d^0 transition metals. Journal of Solid State Chemistry, 115, 395–406.

Kurtz, A.C., Derry, L.A., Chadwick, O.A., and Alfano, M.J. (2000) Refractory element mobility in volcanic soils. Geology, 28, 683–686.

Lebernegg, S., Amthauer, G., and Grodzicki, M. (2008) Single-centre MO theory of transition metal complexes. Journal of Physics B: Atomic, Molecular and Optical Physics, 41, 035102.

Lee, M.J., Lee, J.I., Garcia, D., Moutte, J., Williams, C.T., Wall, F., and Kim, Y. (2006) Pyrochlore chemistry from the Sokli phoscorite-carbonatite complex, Finland: Implications for the genesis of phoscorite and carbonatite association. Geochemical Journal, 40, 1–13.

Lian, Z., Liu, F., He, H., and Liu, K. (2015) Nb-doped VO_x/CeO_2 catalyst for NH_3-SCR of NO_x at low temperatures. RSC Advances, 5, 37675–37681.

Linnen, R.L., and Cuney, M. (2005) Granite-related rare-element deposits and experimental constraints on Ta-Nb-W-Sn-Zr-Hf mineralization, 45–68. In R.L. Linnen and I.M. Samson, Eds., Rare-Element Geochemistry and Mineral Deposits, 17, p. 45–68. Geological Association of Canada Short Course Notes, St. John's, NL, Canada.

Lottermoser, B.G., and England, B.M. (1988) Compositional variation in pyrochlores from the Mt Weld carbonatite laterite, Western Australia. Mineralogy and Petrology, 38, 37–51.

Lü, X., Mou, X., Wu, J., Zhang, D., Zhang, L., Huang, F., Xu, F., and Huang, S. (2010) Improved-performance dye-sensitized solar cells using Nb-doped TiO_2 electrodes: Efficient electron injection and transfer. Advanced Functional Materials, 20, 509–515.

Ma, J., Guo, X., Xue, H., Pan, K., Liu, C., and Pang, H. (2020) Niobium/tantalum-based materials: Synthesis and applications in electrochemical energy storage. Chemical Engineering Journal, 380, 122428.

MacLean, W.H., and Barrett, T.J. (1993) Lithogeochemical techniques using immobile elements. Journal of Geochemical Exploration, 48, 109–133.

Mitchell, R.H. (2015) Primary and secondary niobium mineral deposits associated with carbonatites. Ore Geology Reviews, 64, 626–641.

Nabi, M.M., Wang, J., Meyer, M., Croteau, M.-N., Ismail, N., and Baalousha, M. (2021) Concentrations and size distribution of TiO_2 and Ag engineered particles in five wastewater treatment plants in the United States. Science of the Total Environment, 753, 142017.

Neumann, R., and Medeiros, E.B. (2015) Comprehensive mineralogical and technological characterisation of the Araxá (SE Brazil) complex REE (Nb-P) ore, and the fate of its processing. International Journal of Mineral Processing, 144, 1–10.

Newville, M. (2013) Larch: An analysis package for XAFS and related spectroscopies. Journal of Physics: Conference Series, 430, 012007.

Ogasawara, K., Iwata, T., Koyama, Y., Ishii, T., Tanaka, I., and Adachi, H. (2001) Relativistic cluster calculation of ligand-field multiplet effects on cation $L_{2,3}$ *X*-ray-absorption edges of $SrTiO_3$, NiO, and CaF_2. Physical Review B, 64, 115413.

Okada, K., and Kotani, A. (1993) Theory of core level X-ray photoemission and photoabsorption in Ti compounds. Journal of Electron Spectroscopy and Related Phenomena, 62, 131–140.

Olegário, R.C., Ferreira de Souza, E.C., Marcelino Borges, J.F., Marimon da Cunha, J.B., Chaves de Andrade, A.V., Masetto Antunes, S.R., and Antunes, A.C. (2013) Synthesis and characterization of Fe^{3+} doped cerium–praseodymium oxide pigments. Dyes and Pigments, 97, 113–117.

Oliveira, L.C.A., Ramalho, T.C., Souza, E.F., Gonçalves, M., Oliveira, D.Q.L., Pereira, M.C., and Fabris, J.D. (2008) Catalytic properties of goethite prepared in the presence of Nb on oxidation reactions in water: Computational and experimental studies. Applied Catalysis B: Environmental, 83, 169–176.

Piilonen, P.C., Farges, F., Linnen, R.L., Brown, G.E., Pawlak, M., and Pratt, A. (2006) Structural environment of Nb^{5+} in dry and fluid-rich (H_2O,F) silicate glasses: A combined XANES and EXAFS study. The Canadian Mineralogist, 44, 775–794.

Retegan, M. (2019) Crispy: v0.7.3, doi:10.5281/zenodo.1008184.

Ribeiro, J.M., Correia, F.C., Kuzmin, A., Jonane, I., Kong, M., Goñi, A.R., Reparaz, J.S., Kalinko, A., Welter, E., and Tavares, C.J. (2020) Influence of Nb-doping on the local structure and thermoelectric properties of transparent TiO_2:Nb thin films. Journal of Alloys and Compounds, 838, 155561.

Ruck, R., Babkine, J., Nguyen, C., Marnier, G., and Dusausoy, Y. (1986) Geochemical association of Fe and Nb in synthetic and natural cassiterites and rutiles. Proceedings of experimental mineralogy and geochemistry, p. 122–123. Nancy, France.

Rudnick, R.L. and Gao, S. (2003) Composition of the continental crust. In H.D. Holland and K.K. Turekian, Eds., The Crust, 3, p.1–64. Treatise on Geochemistry, Elsevier-Pergamon, Oxford, U.K.

Schaefers, F., Mertin, M., and Gorgoi, M. (2007) KMC-1: A high resolution and high flux soft X-ray beamline at BESSY. Review of Scientific Instruments, 78, 123102.

Schaube, M., Merkle, R., and Maier, J. (2019) Oxygen exchange kinetics on systematically doped ceria: a pulsed isotope exchange study. Journal of Materials Chemistry A, 7, 21854–21866.

Schulz, K.J., Piatak, N.M., and Papp, J.F. (2017) Niobium and tantalum. In K.J. Schulz, J.H. Jr. DeYoung, R.R. II. Seal, D.W. Bradley., Eds., Critical mineral resources of the United States, U.S. Geological Survey, Professional Paper 1802-M, 34 p.

Shannon, R.D. (1976) Revised effective ionic radii and systematic studies of interatomic distances in halides and chaleogenides. Acta Crystallographica Section B Structural Crystallography and Crystal Chemistry, A32, 751–767.

Sheppard, L., Bak, T., Nowotny, J., Sorrell, C.C., Kumar, S., Gerson, A.R., Barnes, M.C., and Ball, C. (2006) Effect of niobium on the structure of titanium dioxide thin films. Thin Solid Films, 510, 119–124.

Silva, A.C., Oliveira, D.Q.L., Oliveira, L.C.A., Anastácio, A.S., Ramalho, T.C., Lopes, J.H., Carvalho, H.W.P., and Torres, C.E.R. (2009) Nb-containing hematites $Fe_{2-x}Nb_xO_3$: The role of Nb^{5+} on the reactivity in presence of the H_2O_2 or ultraviolet light. Applied Catalysis A: General, 357, 79–84.

Singh, S.K., Eng, J., Atanasov, M., and Neese, F. (2017) Covalency and chemical bonding in transition metal complexes: An ab initio based ligand field perspective. Coordination Chemistry Reviews, 344, 2–25.

Sugiura, C., Kitamura, M., and Mijramatsu, S. (1988) Niobium L_{III} and L_{II} X-ray absorption-edge spectra of Nb_2O_5 and NH_4NbF_6. Journal of Physics and Chemistry of Solids, 49, 1095–1099.

Usui, H., Yoshioka, S., Wasada, K., Shimizu, M., and Sakaguchi, H. (2015) Nb-doped rutile TiO_2: A potential anode material for Na-ion battery. ACS Applied Materials & Interfaces, 7, 6567–6573.

Vantelon, D., Trcera, N., Roy, D., Moreno, T., Mailly, D., Guilet, S., Metchalkov, E., Delmotte, F., Lassalle, B., Lagarde, P., and others (2016) The LUCIA beamline at SOLEIL. Journal of Synchrotron Radiation, 23, 635–640.

Vercamer, V., Hunault, M.O.J.Y., Lelong, G., Haverkort, M.W., Calas, G., Arai, Y., Hijiya, H., Paulatto, L., Brouder, C., Arrio, M.-A., and others (2016) Calculation of optical and K pre-edge absorption spectra for ferrous iron of distorted sites in oxide crystals. Physical Review B, 94, 245115.

Wall, F., Williams, C.T., Woolley, A.R., and Nasraoui, M. (1996) Pyrochlore from weathered carbonatite at Lueshe, Zaire. Mineralogical Magazine, 60, 731–750.

Walter, B.F., Parsapoor, A., Braunger, S., Marks, M.A.W., Wenzel, T., Martin, M., and Markl, G. (2018) Pyrochlore as a monitor for magmatic and hydrothermal processes in carbonatites from the Kaiserstuhl volcanic complex (SW Germany). Chemical Geology, 498, 1–16.

Wang, B., Zhao, Y., Banis, M.N., Sun, Q., Adair, K.R., Li, R., Sham, T.-K., and Sun, X. (2018) Atomic layer deposition of lithium niobium oxides as potential solid-state electrolytes for lithium-ion batteries. ACS Applied Materials & Interfaces, 10, 1654–1661.

Wang, S., Song, Z., Kong, Y., Xia, Z. and Liu, Q. (2018) Crystal field splitting of $4f^{n-1}5d$-levels of Ce^{3+} and Eu^{2+} in nitride compounds. Journal of Luminescence, 194, 461–466.

Waring, J.L., Roth, R.S., and Parker, H.S. (1973) Temperature-pressure phase relationships in niobium pentoxide. Journal of Research of the National Bureau of Standards Section A: Physics and Chemistry, 77A, 705.

Weng, T.-C., Waldo, G.S., and Penner-Hahn, J.E. (2005) A method for normalization of X-ray absorption spectra. Journal of Synchrotron Radiation, 12, 506–510.

Wu, B., Hu, Y.-Q., Bonnetti, C., Xu, C., Wang, R.-C., Zhang, Z.-S., Li, Z.-Y., and Yin, R. (2021) Hydrothermal alteration of pyrochlore group minerals from the Miaoya carbonatite complex, central China and its implications for Nb mineralization. Ore Geology Reviews, 132, 104059.

Yashiro, K. (2004) Electrical properties and defect structure of niobia-doped ceria. Solid State Ionics, 175, 341–344.

Zietlow, P., Beirau, T., Mihailova, B., Groat, L.A., Chudy, T., Shelyug, A., Navrotsky, A., Ewing, R.C., Schlüter, J., Škoda, R., and others (2017) Thermal annealing of natural, radiation-damaged pyrochlore. Zeitschrift für Kristallographie - Crystalline Materials, 232(1-3), 25–38.

FIGURE CAPTIONS

Figure 1: (a) Niobium L_3- and (b) L_2-edge XANES spectra of the studied Nb minerals. The coordination number of Nb ($^{[8]}$Nb and $^{[6]}$Nb) is specified. Vertical lines centered at 2372, 2376, 2387 eV at the L_3-edge and at 2466, 2470, 2481 eV at the L_2-edge evidence the variable position of the B_3 and B_2 features. The spectra of niocalite, lueshite, Nb-substituted hematite and goethite were trimmed beyond 2475 eV due to sulfur impurities resulting in an intense S *K*-edge feature at 2481 eV.

Figure 2: Deconvolution of Nb L_3-XANES spectra of (a) fluorcalciopyrochlore, (b) hydropyrochlore, (c) Nb-substituted hematite, (d) Nb-substituted goethite, (e) Nb-substituted rutile, (f) Nb-substituted anatase, (g) Nb-substituted cerianite, (h) Nb perovskite with three pseudo-Voigts (PV1, PV2, PV3) and an error function (ERF). The experimental (Exp.) and the fitted data (Fit.) correspond to the black and purple curves. All spectra are satisfactorily fitted using this procedure ($\chi^2 < 0.5$), but the fits of Nb-substituted anatase and Nb perovskite spectra are of poorer quality ($\chi^2 = 0.41$ and 0.39, respectively) due to the broadening of B_3 features (Figs. 2f and 2h). The deconvolution of the other XANES spectra is shown in Supplemental Material (Supplemental Figs. S4 and S5).

Figure 3: Comparison of experimental (black dashed lines) and simulated spectra (red lines) obtained by crystal field multiplet (CFM) calculations of (a) Nb-substituted cerianite, (b) Nb-substituted hematite, (c) hydropyrochlore, (d) Nb perovskite. The thin red lines indicate the position and intensity of the electronic transitions when experimental and core-hole lifetime broadenings are absent. The t_{2g} and e_g terms used in the single-particle approach are employed in a matter of clarity but they correspond to the convolution of multi-electronic states.

Figure 4: Comparison of experimental (black dashed lines) and simulated spectra (red lines) obtained by ligand-field multiplet (LFM) calculations of Nb-substituted hematite spectra.

Figure 5: Experimental spectra of Nb perovskite (black spectra) and theoretical spectra depicting the influence of hydridization strength (V_{mix} parameter varying from 0.0 to 5.0 eV with a 0.25 eV step) on the Nb $L_{2,3}$-edges spectral shapes. The arrows mark the low intensity features resulting from charge-transfer effect. Charge-transfer parameters are 3.0, 6.0 and 4.0 eV for U_{dd}, U_{dc} and Δ, respectively.

Figure 6: Dependence between the energy splitting (ΔE parameter) at the L_3-edge and the expected average distance (R) between $^{[6]}$Nb–O or between Fe–O, Ti–O, Ce–O in the case of Nb-substituted reference materials. Experimental data are best fitted with a function proportional to R^{-3} ($\chi^2 = 0.17$), rather than a function proportional to R^{-5} ($\chi^2 = 0.26$). Experimental data corresponding to Nb-substituted Ti oxides deviate from both models. The error bars on ΔE correspond to the instrumental resolution of 0.25 eV at the Nb $L_{2,3}$-edges.

This is the peer-reviewed, final accepted version for American Mineralogist, published by the Mineralogical Society of America.
The published version is subject to change. Cite as Authors (Year) Title. American Mineralogist, in press.
DOI: https://doi.org/10.2138/am-2022-8293. http://www.minsocam.org/

Table 1

Table 1. Structural and chemical information on the selected Nb minerals. (i), (ii) and (iii) correspond to the three groups of Nb minerals described in the main text. Commercial Nb_2O_5 was also selected as a reference material. The cation–O distances are Nb–O except for Ti, Fe and Ce oxides which correspond to Ti–O, Fe–O and Ce–O distances. The site symmetry is that of Nb sites in Nb-bearing minerals and of Fe, Ti and Ce in Fe, Ti and Ce oxides, respectively. The distortion index is calculated as defined by Baur (1974). The references giving the structure of each compound can be found in the Supplemental Material.

Mineral (groups i,ii,iii)	Ideal formula	Structure	Coordination number	Site symmetry (Nb, Ti, Fe, Ce)	Average cation–O distances (Å)	Distortion index (%)	Location
Natural samples							
(i) Fluorcalciopyrochlore	$(Ca,Na)_2(Nb,Ti)_2O_6F$	Corner-sharing NbO_6 octahedra sharing edges with A site cation	6	D_{3d}	1.944	0.0	Tatarka. Russia (SU)
(i) Hydropyrochlore	$(H_2O, □)Nb_2(O.OH)_6(H_2O)$	Corner-sharing NbO_6 octahedra sharing edges with A site cation	6	D_{3d}	1.972	0.0	Lueshe. Congo (SU)
(i) Columbite-(Mn)	$(Mn,Fe)(Nb,Ta)_2O_6$	Chains of edge-sharing NbO_6 octahedra	6	C_1	2.017	6.0	Musha. Rwanda (ENSMP)
(ii) Niobian perovskite	$CaTi_{1-2x}Fe_xNb_xO_3$	Perovskite structure (ABO_3) with interconnected NbO_6 octahedra with interstitial Ca	6	C_1	1.966	0.6	Oka. Canada (ENSMP)
(ii) Niocalite	$Ca_7Nb(Si_4O_{14})O_3F$	Isolated NbO_6 octahedra sharing edges and corners with CaO_6 octahedra	6	C_1	2.049	6.1	Oka. Canada (ENSMP)
Synthetic samples							
(ii) Lueshite	$NaNbO_3$	Perovskite structure (ABO_3) with interconnected NbO_6 octahedra with interstitial Na	6	C_1	1.990	2.8	
(iii) Rutile (5 wt% Nb)	TiO_2	Edge and corner-sharing TiO_6 octahedra (2 edges are shared with each other)	6	D_{2h}	1.956	0.6	
(iii) Anatase (5 wt% Nb)	TiO_2	Edge-sharing TiO_6 octahedra (4 edges are shared with each other)	6	D_{2d}	1.949	1.0	
(iii) Hematite (1 wt% Nb)	α-Fe_2O_3	Face and edge-sharing FeO_6 octahedra	6	C_3	2.031	4.2	
(iii) Goethite (1 wt% Nb)	α-FeOOH	Chains of edge-sharing FeO_6 octahedra joined by corner-sharing FeO_6	6	C_s	2.026	3.8	
(iii) Cerianite (1 wt% Nb)	CeO_2	Edge-sharing CeO_8 cubes	8	O_h	2.343	0.0	
Nb_2O_5	Nb_2O_5	Edge and corner-sharing NbO_6 octahedra. 1 out of 28 Nb sites is a tetrahedron	6	C_1	2.014	1.5	

This is the peer-reviewed, final accepted version for American Mineralogist, published by the Mineralogical Society of America.
The published version is subject to change. Cite as Authors (Year) Title. American Mineralogist, in press.
DOI: https://doi.org/10.2138/am-2022-8293. http://www.minsocam.org/

Table 2

Table 2. Summary of the parameters obtained from the fitting procedure including the energy splitting between the features A and B (ΔE), the relative intensity ratios (I_A/I_B) and the ratio of the B feature width with respect to A feature ($FWHM_{B/A}$). The quality of the fit is assessed using the Pearson chi-squared test (χ^2). The amplitude, center, width and intensity of the pseudo-Voigts can be found in Supplemental Table S3.

	L_3-edge				L_2-edge			
Sample	**ΔE (eV)**	**I_A/I_B**	**$FWHM_{B/A}$**	**χ^2**	**ΔE (eV)**	**I_A/I_B**	**$FWHM_{B/A}$**	**χ^2**
Nb cerianite	2.55	0.75	1.47	0.06	2.29	0.96	1.73	0.06
Nb_2O_5	3.28	0.94	1.73	0.04	3.06	1.24	1.92	0.04
Fluorcalciopyrochlore	3.90	1.18	1.48	0.09	3.83	1.55	1.69	0.06
Hydropyrochlore	3.76	1.07	1.62	0.05	3.64	1.41	1.67	0.04
Columbite	3.41	1.11	1.48	0.06	3.32	1.47	1.73	0.06
Niocalite	3.43	1.17	1.38	0.11	3.44	1.55	1.63	0.10
Lueshite	3.54	1.05	1.68	0.08	3.75	1.42	1.28	0.09
Nb perovskite	3.96	1.20	2.08	0.39	3.95	1.60	2.35	0.16
Nb hematite	3.44	1.08	1.12	0.28	3.47	1.45	1.39	0.10
Nb goethite	3.46	1.08	1.18	0.25	3.48	1.46	1.47	0.11
Nb anatase 1% Nb	3.38	1.10	1.58	0.51	3.30	1.48	1.84	0.19
Nb anatase 5% Nb	3.34	1.14	1.62	0.41	3.29	1.55	1.88	0.17
Nb anatase 10% Nb	3.33	1.14	1.61	0.39	3.28	1.55	1.92	0.15
Nb rutile 5% Nb	3.45	1.03	1.54	0.21	3.31	1.25	1.78	0.09

This is the peer-reviewed, final accepted version for American Mineralogist, published by the Mineralogical Society of America.
The published version is subject to change. Cite as Authors (Year) Title. American Mineralogist, in press.
DOI: https://doi.org/10.2138/am-2022-8293. http://www.minsocam.org/

Table 3. Crystal-field multiplet (CFM) parameters that best reproduce the experimental spectra.

Sample	Nb point group symmetry	Slater integrals reduction	10*Dq* (eV)
Nb-substituted cerianite	O_h	0.51	2.80
Nb-substituted hematite	O_h	0.51	3.70
Hydropyrochlore	O_h	0.54	3.90
Nb perovskite	O_h	0.35	3.90

This is the peer-reviewed, final accepted version for American Mineralogist, published by the Mineralogical Society of America.
The published version is subject to change. Cite as Authors (Year) Title. American Mineralogist, in press.
DOI: https://doi.org/10.2138/am-2022-8293. http://www.minsocam.org/

Table 4. Crystal-field and charge-transfer parameters that best reproduce the experimental spectra.

Sample	Nb point group symmetry	Slater integrals reduction	$10Dq$ (eV)	U_{dd} (eV)	U_{dc} (eV)	Δ (eV)	V_{eg} (eV)	V_{t2g} (eV)
Nb-substituted hematite	O_h	0.70	2.25	2.0	6.0	4.0	4.0	-2.0

This is the peer-reviewed, final accepted version for American Mineralogist, published by the Mineralogical Society of America.
The published version is subject to change. Cite as Authors (Year) Title. American Mineralogist, in press.
DOI: https://doi.org/10.2138/am-2022-8293. http://www.minsocam.org/

Fig. 1

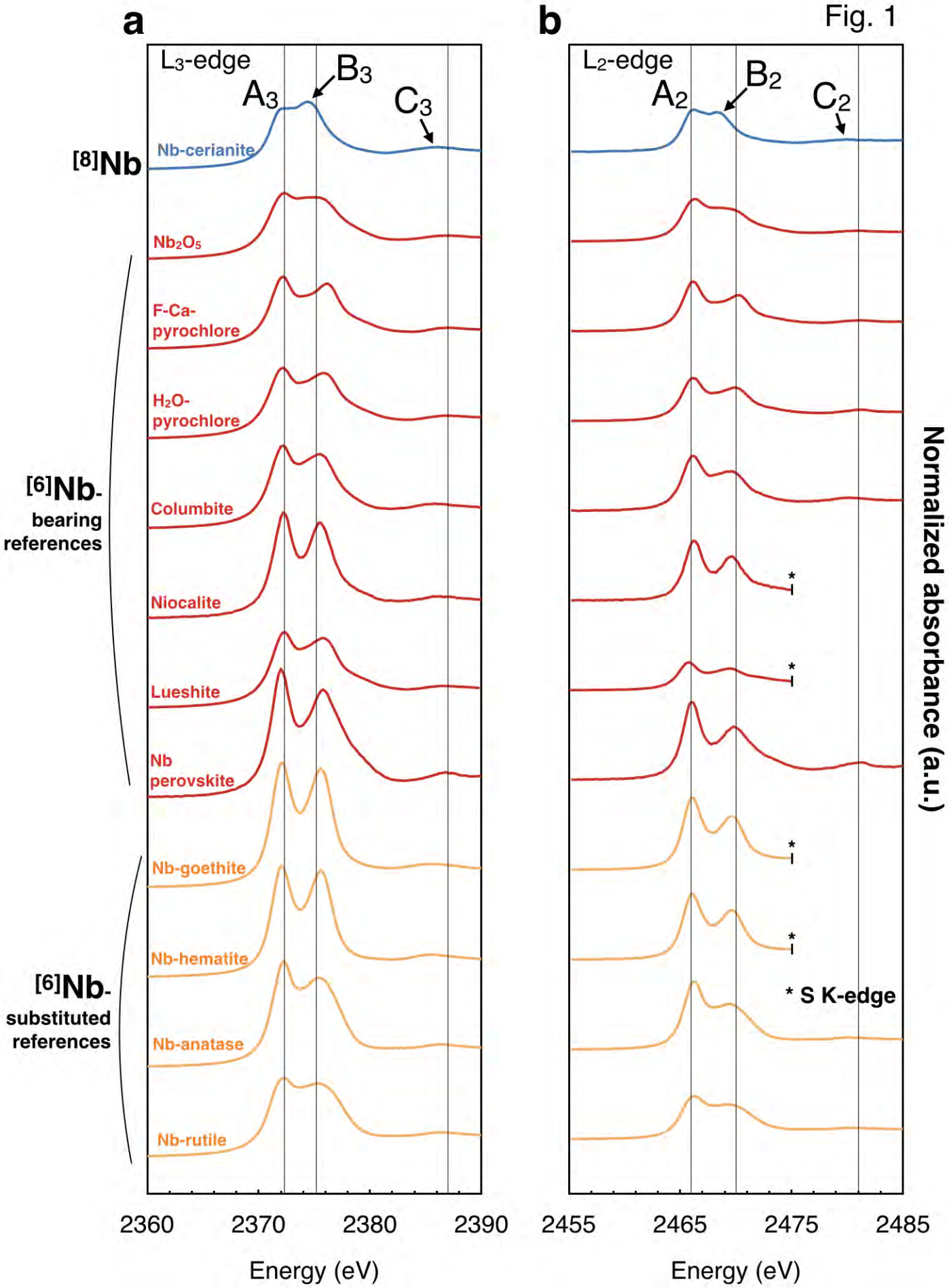

This is the peer-reviewed, final accepted version for American Mineralogist, published by the Mineralogical Society of America.
The published version is subject to change. Cite as Authors (Year) Title. American Mineralogist, in press.
DOI: https://doi.org/10.2138/am-2022-8293. http://www.minsocam.org/

Fig. 2

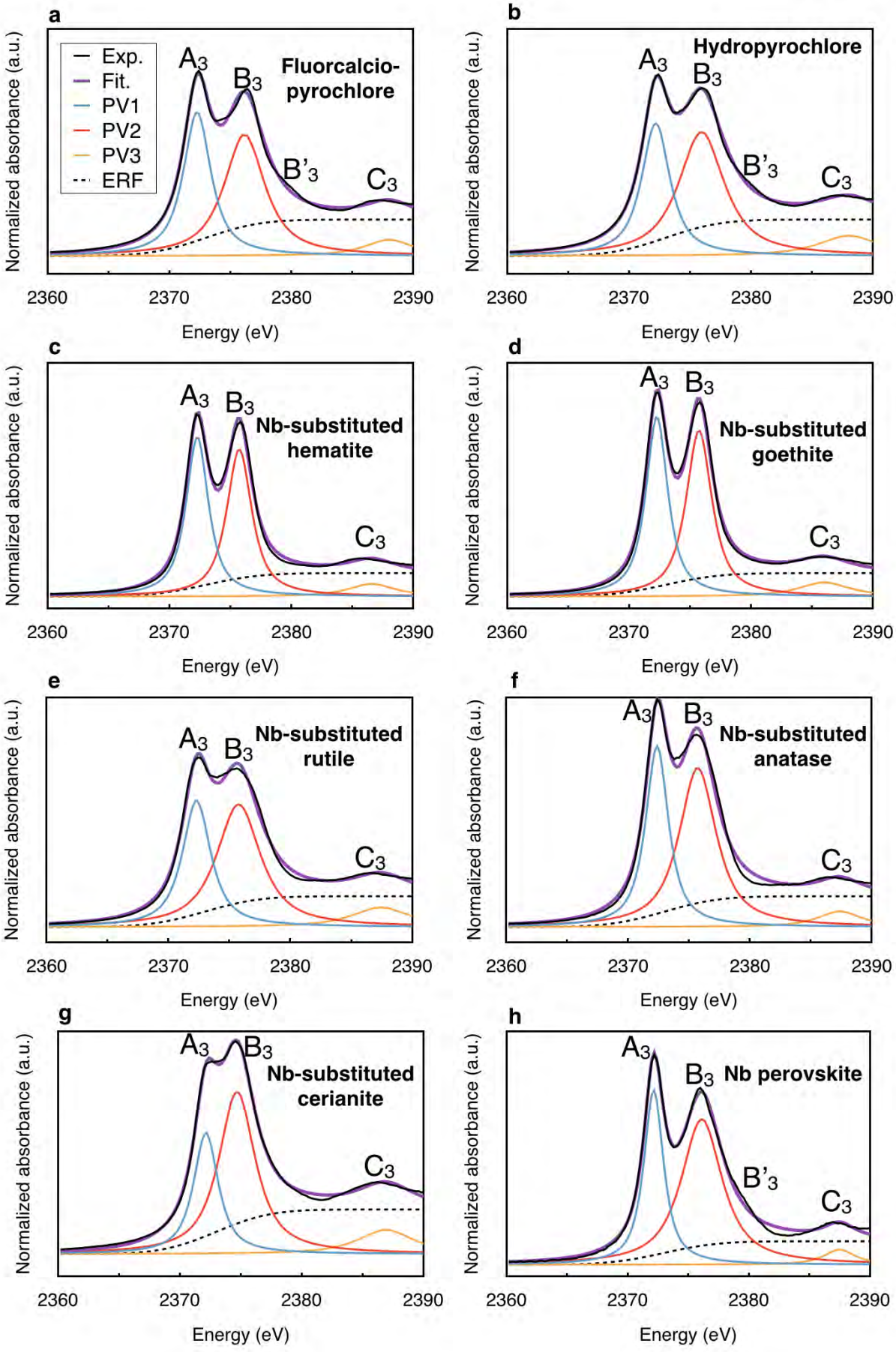

This is the peer-reviewed, final accepted version for American Mineralogist, published by the Mineralogical Society of America.
The published version is subject to change. Cite as Authors (Year) Title. American Mineralogist, in press.
DOI: https://doi.org/10.2138/am-2022-8293. http://www.minsocam.org/

Fig. 3

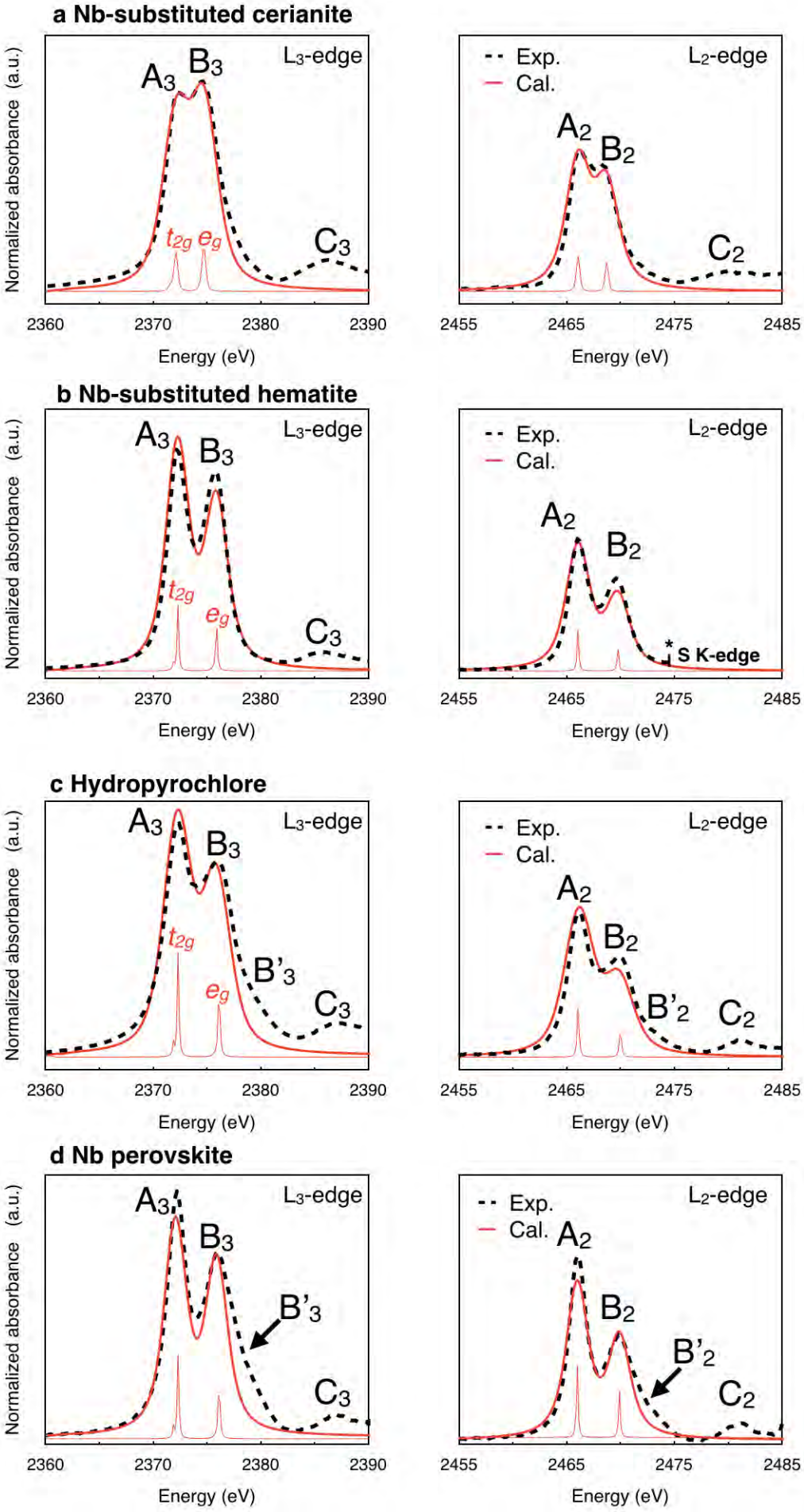

This is the peer-reviewed, final accepted version for American Mineralogist, published by the Mineralogical Society of America.
The published version is subject to change. Cite as Authors (Year) Title. American Mineralogist, in press.
DOI: https://doi.org/10.2138/am-2022-8293. http://www.minsocam.org/

Fig. 4

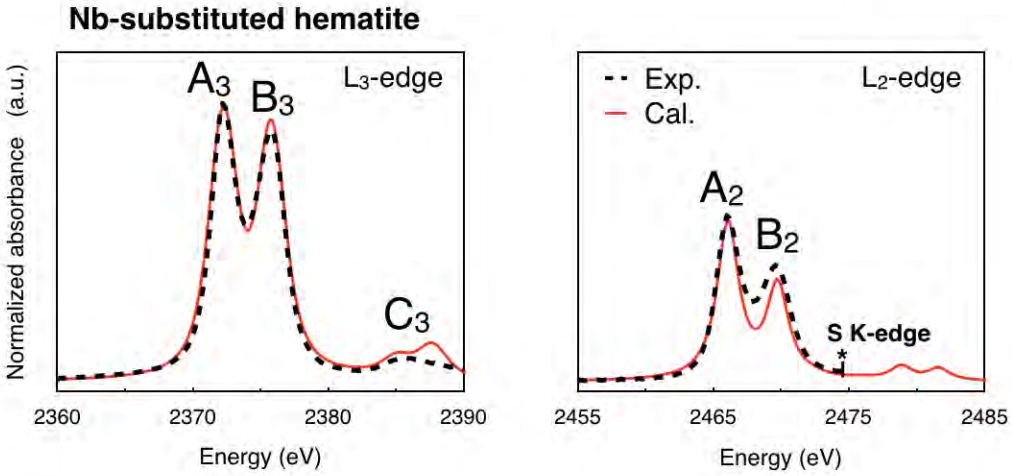

This is the peer-reviewed, final accepted version for American Mineralogist, published by the Mineralogical Society of America.
The published version is subject to change. Cite as Authors (Year) Title. American Mineralogist, in press.
DOI: https://doi.org/10.2138/am-2022-8293. http://www.minsocam.org/

Fig. 5

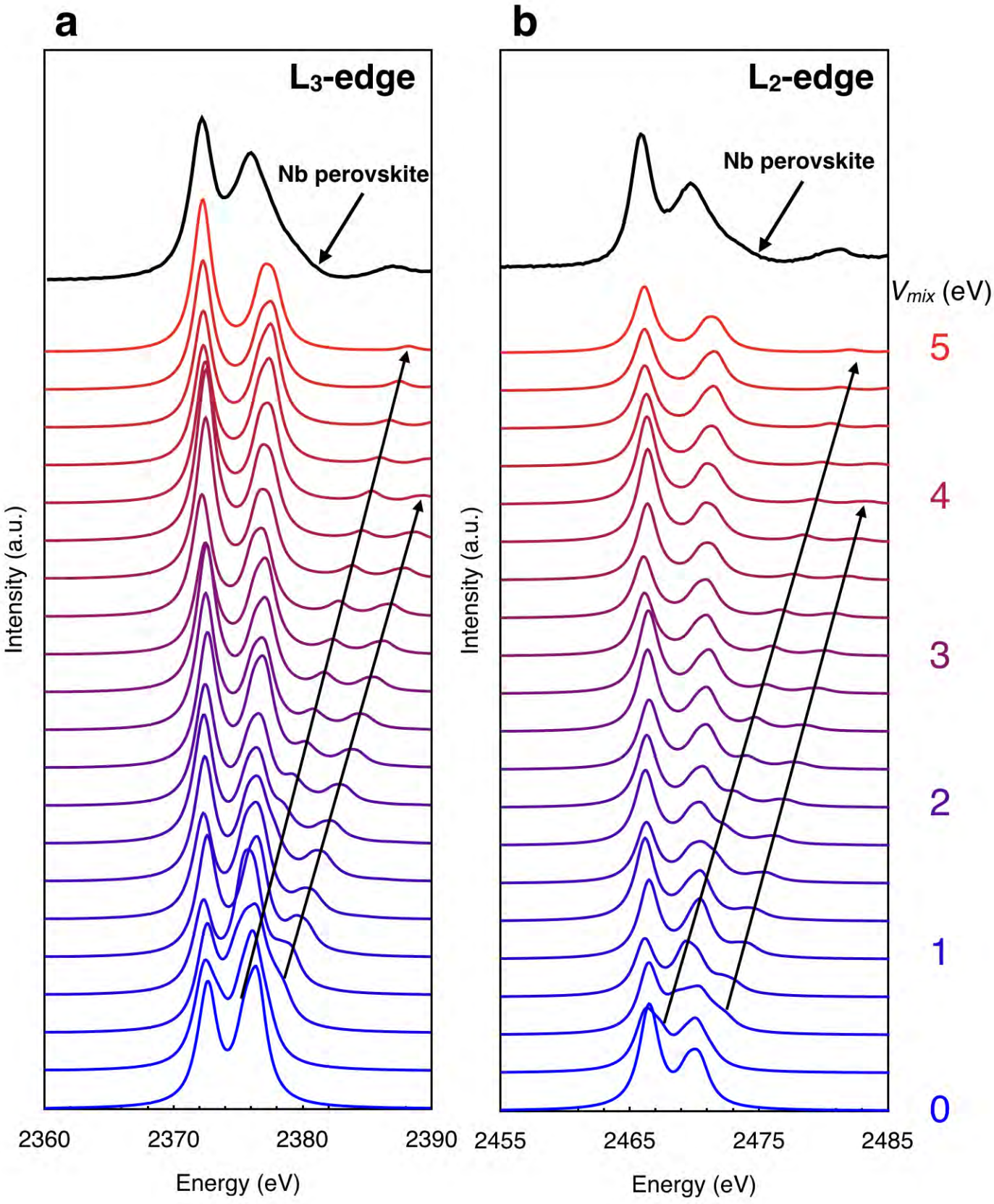

Fig. 6